

Theory of wave propagation in partially saturated double-porosity rocks: a triple-layer patchy model

Weitao Sun,^{1,2} Jing Ba³ and José M. Carcione⁴

¹Zhou Pei-Yuan Center for Applied Mathematics, Tsinghua University, Beijing, 100084, China

²State Key Laboratory of Petroleum Resources and Prospecting, China University of Petroleum, Beijing, 102249, China

³Department of Computational Geophysics, Xi'an Jiaotong University, Xi'an, 710049, China. E-mail: baj04@mails.tsinghua.edu.cn

⁴Istituto Nazionale di Oceanografia e di Geofisica Sperimentale (OGS), Borgo Grotta Gigante 42c, Sgonico, Trieste I-34010, Italy

Accepted 2015 December 23. Received 2015 December 22; in original form 2015 August 21

SUMMARY

Wave-induced local fluid flow is known as a key mechanism to explain the intrinsic wave dissipation in fluid-saturated rocks. Understanding the relationship between the acoustic properties of rocks and fluid patch distributions is important to interpret the observed seismic wave phenomena. A triple-layer patchy (TLP) model is proposed to describe the *P*-wave dissipation process in a double-porosity media saturated with two immiscible fluids. The double-porosity rock consists of a solid matrix with unique host porosity and inclusions which contain the second type of pores. Two immiscible fluids are considered in concentric spherical patches, where the inner pocket and the outer sphere are saturated with different fluids. The kinetic and dissipation energy functions of local fluid flow (LFF) in the inner pocket are formulated through oscillations in spherical coordinates. The wave propagation equations of the TLP model are based on Biot's theory and the corresponding Lagrangian equations. The *P*-wave dispersion and attenuation caused by the Biot friction mechanism and the local fluid flow (related to the pore structure and the fluid distribution) are obtained by a plane-wave analysis from the Christoffel equations. Numerical examples and laboratory measurements indicate that *P*-wave dispersion and attenuation are significantly influenced by the spatial distributions of both, the solid heterogeneity and the fluid saturation distribution. The TLP model is in reasonably good agreement with White's and Johnson's models. However, differences in phase velocity suggest that the heterogeneities associated with double-porosity and dual-fluid distribution should be taken into account when describing the *P*-wave dispersion and attenuation in partially saturated rocks.

Key words: Microstructure; Permeability and porosity; Body waves; Seismic attenuation; Wave propagation; Acoustic properties.

1 INTRODUCTION

In seismic propagation, wave attenuation can be caused by scattering and intrinsic mechanisms. The latter has been found to dominate the scattering loss at all frequencies for a stratified sequence of water-saturated sandstones, siltstones and limestones (Sams *et al.* 1997). Cross-well experiments suggest that at seismic frequencies scattering loss is negligible compared with intrinsic attenuation (Quan & Harris 1997). It is believed that intrinsic attenuation is mainly caused by wave-induced local fluid flow in fluid-saturated rocks. In response to a passing *P* wave, the porous solid skeleton is compressed and dilated. In reality, skeletons and saturating fluid distributions are spatially heterogeneous, which causes spatial gradients in fluid pressure and introduces fluid flow. Fluid movements relative to the rock frame create internal frictions until the pore pressure is equilibrated.

The macroscopic flow at the wavelength scale was first studied by Biot (1956a,b). Biot theory quantifies the viscous-inertial attenuation and gives frequency-dependent velocities. However, the 'Biot loss' underestimates the measured attenuation in many cases in the seismic band (Mochizuki 1982; Dvorkin *et al.* 1995; Arntsen & Carcione 2001). A microscopic 'squirt flow' mechanism has then been proposed to account for the measured high attenuation and velocity dispersion (Oconnell & Budiansky 1977; Mavko & Nur 1979; Dvorkin *et al.* 1995; Thas 2007), by which compliance differences between adjacent pores, originating in pore-shape orientations, causes local pressure gradients of pore fluid. The microcracks and grain contacts show a greater deformation than the intergranular pores, responding with a greater fluid

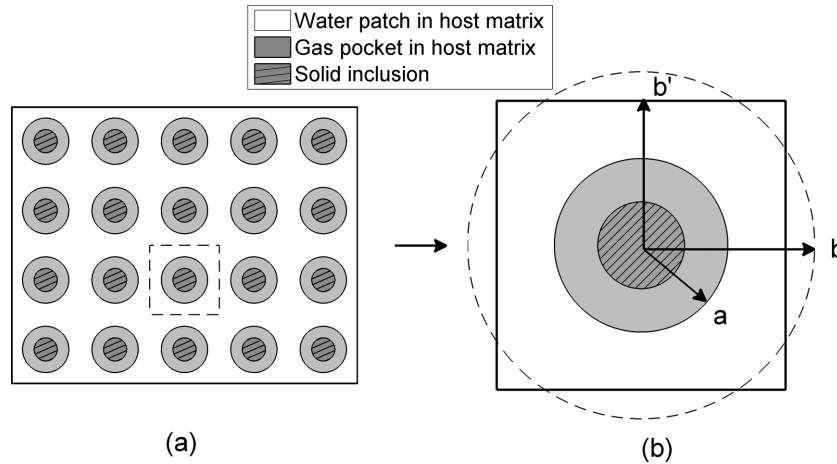


Figure 1. Heterogeneities in solid matrix and fluid patch. (a) Spatial distribution of less consolidated inclusions and gas pocket in host matrix. (b) Concentric spherical model with less consolidated solid inclusion (hatched line area) embedded in a consolidated host sphere (radius b) and gas pocket (grey shaded area with radius a) embedded in a host water patch (blank shell with radius b).

pressure than the main pore space and resulting in a squirt flow from cracks to pores. The squirt-flow model is able to explain the measured attenuation at ultrasonic frequencies, but mostly fails in the seismic band (Pride *et al.* 2004).

Seismic attenuation is mainly due to the spatial variations in rock compliance on a scale much larger than a typical pore size but much smaller than the wavelength, which is known as mesoscopic inhomogeneity in the frame and fluid distributions. Mesoscopic scale models have been developed to explain the wave dispersion and attenuation in a single-porosity medium saturated by two immiscible fluids (White 1975; Dutta & Odé 1979a,b; Johnson 2001; Pride *et al.* 2004; Ba *et al.* 2011) and in a mixture of two porous phases saturated with a single fluid (White *et al.* 1975; Berryman & Wang 2000; Pride *et al.* 2004; Ba *et al.* 2011; Rubino & Holliger 2012). The inhomogeneous lithology distributions or patches of pore fluids form the mesoscopic heterogeneity, for which the scale is larger than the grain size and smaller than the wavelength. The velocity and attenuation of P waves are strongly dependent upon the fluid distribution and pore geometry within the rock matrix (Nur 1971, 1973; Solomon 1972). Fluids in different porosity respond with different pore pressure increments under waves' squeezing. Internal relaxation leads to local fluid flow between compliant and stiff regions as a compressional wave is passing through. The subsequent flow causes energy loss and account for the attenuation in seismic band.

White (1975) studied P -wave dispersion/attenuation in unconsolidated rocks with partial gas/water saturation. The energy loss mechanism is based on a concentric spherical model with a gas pocket embedded in a liquid sphere. White's work ascribed the P -wave dispersion and attenuation to fluid flow at the mesoscopic level and this is considered as the first patchy saturation model. White *et al.* (1975) considered porous alternating layers, where the medium in each layer is isotropic and partially saturated. Dutta & Odé (1979a,b) and Dutta & Seriff (1979) improved White's spherical patchy model by modifying White's formulas and the corrections gave an expected Gassmann–Wood velocity at very low frequencies. Berryman & Wang (1995) extended Biot's poroelasticity to include fractures/cracks by making a generalization for a double-porosity/dual-permeability model. Berryman & Wang (2000) also applied the double-porosity analysis of poroelasticity to seismic wave propagation. Johnson (2001) developed a generalization of White's model for patches of arbitrary shape by using a branching function approach. Pride *et al.* (2004) provided a unified theoretical treatment for P -wave attenuation models in sedimentary rocks, that is, two mesoscopic heterogeneity models (pore type variations with a single fluid saturating all the pores, a single uniform lithology saturated by two immiscible fluids with mesoscopic 'patches') and a microscopic squirt flow model. Carcione & Picotti (2006) studied the influence of pore fluid and solid frame properties on the dispersion/attenuation curves. Recently, Ba *et al.* (2011) formulated a double-porosity model (Biot–Rayleigh or BR model) based on Biot theory and the dynamics of gas-bubble oscillation in water developed by Rayleigh (1917), where the wave-induced local fluid flow of a spherical inclusion is modeled. Dynamic equations for double-porosity media are obtained and the effective bulk modulus are calculated. Quintal *et al.* (2011) reported a finite element modeling of seismic attenuation and dispersion between regions of different compressibilities described by Biot's equations.

In hydrocarbon reservoirs, the heterogeneity of pore structures lies in the form of matrix pores and cracks. Even in an apparently uniform sandstone formation, a small volume fraction of less consolidated sand grains may be considered as a second type of skeleton. The heterogeneity due to pore-type variations (e.g. mixtures of sands and clays) can interweave with the heterogeneity caused by patches of different immiscible fluids (Fig. 1). Previous attempts to incorporate porosity and fluid heterogeneities into patchy models provide rigorous extensions of the mesoscopic attenuation mechanism (Pride & Berryman 2003b; Ba *et al.* 2011). Some efforts were dedicated to investigate the elastic wave characteristics in nature rocks simultaneously containing patchy-saturation and pore structure heterogeneities, for example, from the angle of view of poroelasticity theory (Ba *et al.* 2015) or from the angle of view of numerical modeling (Rubino & Holliger 2012). In this work, we aim to develop an approach by making the idealization that the mesoscopic heterogeneity can be meaningfully reduced to a triple-layer spherical patchy model.

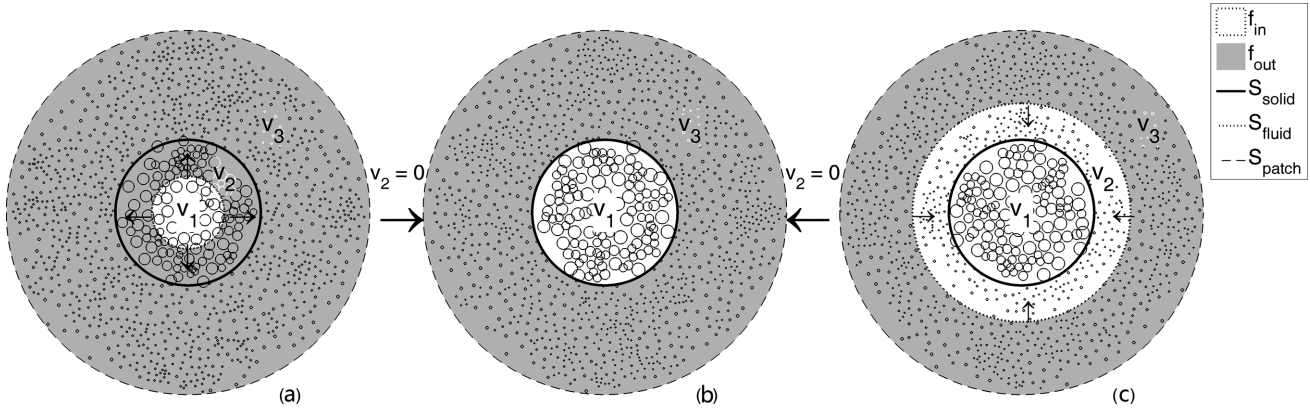


Figure 2. Triple-layer patchy (TLP) model. (a) Fluid-pocket inside inclusion (FII); (b) fluid-pocket completely overlaps inclusion; (c) fluid-pocket cover inclusion (FCI). f_{in} is the inner fluid pocket. f_{out} is the outer fluid. S_{solid} is the solid matrix heterogeneity interface. S_{fluid} is the fluid saturation heterogeneity interface. The volume fractions of the inner pocket, intermediate and outer layers are v_1 , v_2 , v_3 , respectively.

The main goal of this study is to propose a triple-layer patchy (TLP) model to analyze P -wave dissipation processes in a double-porosity medium saturated with two fluids (Fig. 1). The influences of the solid skeleton and the pore-fluid distribution on the P -wave velocity are considered simultaneously. The model consists of spherical inclusions embedded in a homogeneous host medium (see Fig. 1b). The inclusions are homogeneous and their radii are much smaller than the P wavelength but larger than the pore size (in a mesoscopic scale). The interface between inclusions and host medium is open and fluids can flow through it. On the other hand, the skeletons are saturated with two types of fluids. There is an interface between the inner fluid patch and the outside fluid zone (Fig. 1b). The fluid interface is not necessarily related to the interface between inclusion and host medium. As a matter of fact, the solid matrix and pore fluid patch are two independent heterogeneous systems and are treated separately. Based on such a ‘triple-layer patchy’ idealization, analytical solutions are obtained in the form of differential equations and measurable coefficients.

The formulation requires to know: (i) the strain energy of the partially-saturated double-porosity rock system (the TLP model); (ii) the kinetic energy of the TLP model and (iii) the dissipation functions of the TLP model. We obtain the wave propagation equations by substituting the energies and dissipation functions into the Euler-Lagrange equation. The analysis differs from single porosity energy treatments in two aspects: (i) we express the fluid flow kinetic energy in terms of the global and local fluid flows and (ii) we obtain the dissipation related to both fluid flows. The kinetic energy of the local fluid flow is derived by means of a spherical harmonics formulation. Then, the solutions of the wave equation are obtained by a plane-wave analysis.

The paper is organized as follows. Section 2 describes the TLP model incorporating both the skeleton and fluid distribution heterogeneities. We also consider the patch interface vibrations which relate the local fluid flow ζ to the patch size and porosity. In Sections 3 and 4, we derive the strain and kinetic energies of the global fluid flow. In Sections 5 and 6, we derive the dissipation energy functions of the global and local fluid flow. The wave equation is obtained in Section 7 by using the Lagrangian formulation and Section 8 presents the plane-wave solutions. Finally, in Section 9, we compute the P -wave dispersion and attenuation induced by the fluid flow and compare the results to experimental data.

2 INTERFACE VIBRATION AND FLUID EXCHANGE

In this work, solid and fluid heterogeneities are considered simultaneously in the TLP model. The fluid heterogeneity is realized by merging two of the triple concentric layers into one effective layer which is saturated by the same fluid (Fig. 2). The other layer is saturated by another fluid. The whole spherical patch is separated by the fluid interface S_{fluid} , the solid interface S_{solid} and the patch boundary S_{patch} .

The three geometrical layers are represented by subscripts $m = 1, 2, 3$ from the inner pocket to the outer boundary. The volume fractions and porosities of each layer are v_1, v_2, v_3 and $\phi_{10}, \phi_{20}, \phi_{30}$, respectively. The fluids in each layer are represented by f_1, f_2, f_3 correspondingly. We consider two types of porosity: the inclusion porosity ϕ_{in} and the host porosity ϕ_{out} . The inner and outer layer porosities satisfy $\phi_{10} = \phi_{in}$ and $\phi_{20} = \phi_{out}$, while the middle layer porosity is to be determined according to the relative position of the fluid interface S_{fluid} and solid interface S_{solid} . In the same way, we can assign the saturating fluid types for the inner, outer and middle layers.

The matrix and fluid heterogeneities are investigated in two ways. In the first case, the inner fluid pocket is within the solid inclusions (fluid inside inclusion or FII). As a consequence, the solid interface S_{solid} is located outside the fluid interface S_{fluid} (Fig. 2a). Layers 1 and 2 have the same porosity $\phi_{10} = \phi_{20} = \phi_{in}$, and layer 3 has porosity $\phi_{30} = \phi_{out}$. The outer layers 2 and 3 are saturated by the same fluid and combined into one effective layer. Then, we have $\phi_{10} = \phi_{20} \neq \phi_{30}$ and $f_2 = f_3 \neq f_1$. The porosity and volume of the effective layer are $\bar{\phi}_{20}, \bar{v}_2$.

$$\bar{\phi}_2 = \bar{\phi}_{20} \bar{v}_2, \quad (1)$$

$$\bar{v}_2 = v_2 + v_3, \quad (2)$$

$$\bar{\phi}_{20} = \frac{\phi_{20}v_2 + \phi_{30}v_3}{\bar{v}_2}. \quad (3)$$

In the second case (Fig. 2c), the fluid interface S_{fluid} is located outside the solid interface S_{solid} (fluid cover inclusion or FCI). Layers 2 and 3 have the same porosity $\phi_{20} = \phi_{30} = \phi_{\text{out}}$ and layer 3 has porosity $\phi_{10} = \phi_{\text{in}}$. Then, we have $\phi_{20} = \phi_{30} \neq \phi_{10}$ and $f_1 = f_2 \neq f_3$. The inner layers 1 and 2 are saturated by the same fluid and combined into an effective layer with $\bar{\phi}_{10}, \bar{v}_1$. The effective parameters of the combined layers are labeled with a bar.

$$\bar{\phi}_1 = \bar{\phi}_{10}\bar{v}_1, \quad (4)$$

$$\bar{v}_1 = (v_1 + v_2), \quad (5)$$

$$\bar{\phi}_{10} = \frac{\phi_{10}v_1 + \phi_{20}v_2}{\bar{v}_1}. \quad (6)$$

When the fluid interface exactly overlaps the solid inclusion interface (Fig. 2b), that is, $v_2 = 0$, FII and FCI reduce to the same case.

The surfaces of the three layers are assumed to be geometrically spherical with radius r_{10}, r_{20}, r_{30} . When the P -wave propagation causes vibrations, the instantaneous radial positions of the surfaces are indicated by r_1, r_2, r_3 . Considering the wave-induced flow, the fluid being depleted from the inner pocket to the outer domain is $\phi_1\zeta$, and the opposite flow induces the variation $-\phi_2\zeta$, where

$$\zeta = \frac{1}{\phi_2} \left(1 - \frac{r_{10}^3}{r_1^3} \right). \quad (7)$$

ζ is the variation of fluid content, which represents the fluid content increment due to the diffusion across the internal interface separating different phases. Once we assume that the vibration amplitude of the fluid interface is sufficiently small, the radius r_1 can be expanded as

$$r_1 = r_{10}(1 - \phi_2\zeta)^{-\frac{1}{3}} \approx r_{10} + \frac{1}{3}r_{10}\phi_2\zeta. \quad (8)$$

The rate at which the internal interface vibrates is $\dot{r}_1 \approx \frac{1}{3}r_{10}\phi_2\dot{\zeta}$.

3 STRAIN ENERGY

In this section, the strain energy functions of the TLP model are derived. The strain energies for the cases FII and FCI are

$$W_{\text{FII}} = \frac{1}{2}[(A + 2N)I_1^2 - 4NI_2 + 2Q_1I_1(\xi_1 - \bar{\phi}_2\zeta) + R_1(\xi_1 - \bar{\phi}_2\zeta)^2 + 2\bar{Q}_2I_1(\xi_2 + \phi_1\zeta) + \bar{R}_2(\xi_2 + \phi_1\zeta)^2], \quad (9)$$

$$W_{\text{FCI}} = \frac{1}{2}[(A + 2N)I_1^2 - 4NI_2 + 2\bar{Q}_1I_1(\xi_1 - \phi_2\zeta) + \bar{R}_1(\xi_1 - \phi_2\zeta)^2 + 2Q_2I_1(\xi_2 + \bar{\phi}_1\zeta) + R_2(\xi_2 + \bar{\phi}_1\zeta)^2], \quad (10)$$

where $I_1 = e_{11} + e_{22} + e_{33}$ and $I_2 = \frac{1}{2}(e_{11}^2 + e_{22}^2 + e_{33}^2 + 2e_{12}e_{21} + 2e_{13}e_{31} + 2e_{23}e_{32})$ are the first and second strain invariants. Here $e_{ij} = (u_{ij} + u_{ji})/2$ and $u_i (i = 1, 2, 3)$ is the mesoscopic volume average displacement of solid skeleton. The ‘, j ’ subscript represents the spatial derivative with respect to the j -th coordinate.

Here, \mathbf{u} is the mesoscopic volume average displacement of the solid skeleton and ξ_m are the first strain invariants of the average fluid displacement $\mathbf{U}^{(m)} (m = 1, 2)$ in each effective material layer,

$$\xi_m = \varepsilon_{11} + \varepsilon_{22} + \varepsilon_{33}. \quad (11)$$

The fluid strain components are defined as

$$\varepsilon_{ij}^{(m)} = \frac{1}{2}(U_{ij}^{(m)} + U_{ji}^{(m)}). \quad (12)$$

N is the average shear modulus of the solid skeleton. The coefficients $A, Q_m, R_m, \bar{Q}_m, \bar{R}_m (m = 1, 2)$ are stiffnesses, which are functions of the porosity ϕ , the frame bulk modulus K_b , and the solid and fluid bulk moduli K_s, K_f (see the Appendix).

$$A = \left(1 - \sum_{m=1}^2 \phi_m \right) K_s - \frac{2}{3}N - K_s \sum_{m=1}^2 \frac{Q_m}{K_{f_m}}, \quad (13)$$

$$Q_m = \frac{K_s \phi_m}{1 + \gamma_m}, \quad (14)$$

$$R_m = \frac{K_{f_m} \phi_m}{1 + 1/\gamma_m}, \quad m = 1, 2, \quad (15)$$

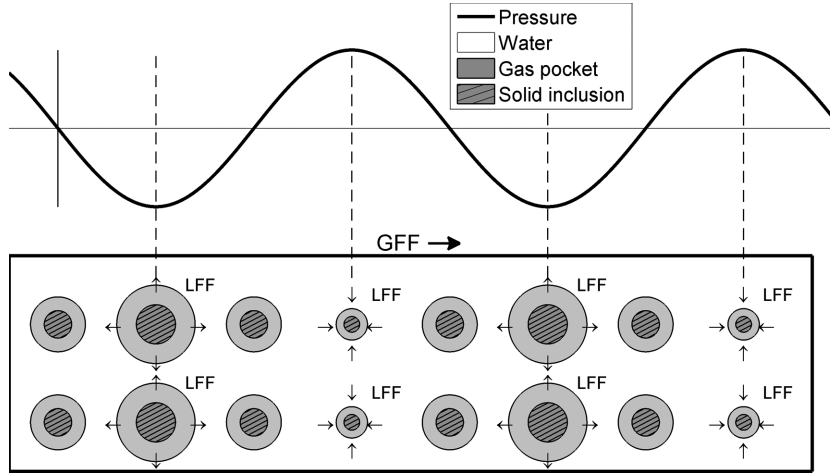


Figure 3. The global fluid flow (GFF) and local fluid flow (LFF) caused by the plane-wave excitation.

$$\gamma_1 = \frac{K_s}{K_{f1}} \left[\frac{\phi_1 + \phi_2 \beta}{1 - K_b/K_s - \sum_{m=1}^2 \phi_m} \right], \quad (16)$$

$$\gamma_2 = \frac{K_s}{\beta K_{f2}} \left[\frac{\phi_1 + \phi_2 \beta}{1 - K_b/K_s - \sum_{m=1}^2 \phi_m} \right], \quad (17)$$

ϕ_m are the porosities of each porous layer phase. Let v_m be the volume fraction of phase m in the averaging volume. Then we have $\phi_m = v_m \phi_{m0}$, where ϕ_{m0} is the porosity in the m -th domain. The total porosity is $\phi = \sum_{m=1}^2 \phi_m$.

4 KINETIC ENERGY

The kinetic energy of the effective system is:

$$T = \frac{1}{2} \left[\rho_0 \sum_{i=1}^3 \dot{u}_i^2 + \sum_{m=1}^2 \int_{\Omega_m} \rho_{f_m} \sum_{i=1}^3 \left(\dot{u}_i + \mathbf{g}_i^{(m)} + \mathbf{l}_i^{(m)} \right)^2 d\Omega_m \right], \quad (18)$$

where $\mathbf{g}^{(m)}$, $\mathbf{l}^{(m)}$ are the global and local relative microvelocity fields of the fluid. The solid skeleton density is ρ_0 , ρ_{f_m} and Ω_m are the fluid densities and fluid volume in the m th domain, respectively.

The direction of global flow caused by the plane-wave excitation is the same as that of the wave propagation. For the static isotropic microvelocity field, the global flow velocity vector is $\mathbf{g}_i^{(m)} = c\phi(\dot{U}_i^{(m)} - \dot{u}_i)$ (Biot 1962; Berryman & Wang 2000). Here c is a coefficient which depends on the pore geometry and we let $c = 1$. The local flow oscillation is assumed to be perpendicular to the inner sphere's surface (Fig. 3). The oscillation amplitude is the same on the sphere surface.

Since \dot{u}_i is the average velocity of the solid skeleton, it can be taken out of the integral. The terms in the kinetic energy are

$$\int_{\Omega_m} \rho_{f_m} \dot{u}_i^2 d\Omega_m = \rho_m \dot{u}_i^2, \quad (19)$$

$$\int_{\Omega_m} \rho_{f_m} 2\dot{u}_i \mathbf{g}_i^{(m)} d\Omega_m = 2\dot{u}_i \int_{\Omega_m} \rho_{f_m} \mathbf{g}_i^{(m)} d\Omega_m = 2\dot{u}_i \rho_m \left(\dot{U}_i^{(m)} - \dot{u}_i \right) = -2\rho_m \dot{u}_i^2 + 2\rho_m \dot{u}_i \dot{U}_i^{(m)}, \quad (20)$$

$$\int_{\Omega_m} \rho_{f_m} \mathbf{g}_i^{(m)2} d\Omega_m = \int_{\Omega_m} \rho_{f_m} a^2 \phi_m^2 \left(\dot{U}_i^{(m)} - \dot{u}_i \right)^2 d\Omega_m = \rho_{mm} \left(\dot{U}_i^{(m)} - \dot{u}_i \right)^2 = \rho_{mm} \dot{u}_i^2 - 2\rho_{mm} \dot{u}_i \dot{U}_i^{(m)} + \rho_{mm} \dot{U}_i^{(m)2}, \quad (21)$$

where ρ_m and ρ_{mm} are density coefficients. Since the local flow vector is perpendicular to the inner sphere surface and has the same amplitude in all radial directions, it can be deduced that (Ba *et al.* 2011)

$$\int_{\Omega_m} \rho_{f_m} \dot{u}_i \mathbf{l}_i^{(m)} d\Omega_m = 0. \quad (22)$$

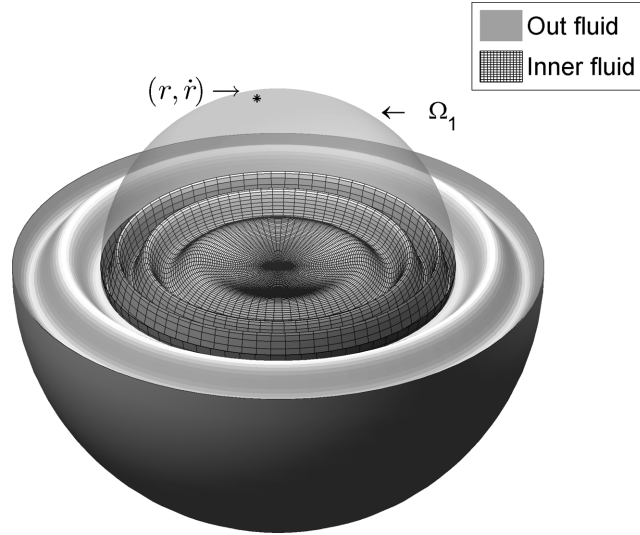


Figure 4. The pocket-shell spherical harmonics model; r and velocity \dot{r} are the fluid displacement and velocity, while Ω_1 is the inner-pocket domain.

For the spherical inclusions with a uniform size, we also have (Ba *et al.* 2011)

$$\int_{\Omega_m} \rho_{f_m} \mathcal{G}_i^{(m)} l_i^{(m)} d\Omega_m = 0. \quad (23)$$

If we define

$$\rho_{00} = \rho_0 - \sum_{m=1}^3 (\rho_m - \rho_{mm}), \quad (24)$$

$$\rho_{0m} = \rho_m - \rho_{mm}, \quad (25)$$

the kinetic energy can be rewritten as

$$T = \frac{1}{2} \sum_{i=1}^3 \rho_{00} \dot{u}_i^2 + \sum_{i=1}^3 \sum_{m=1}^2 \rho_{0m} \dot{u}_i \dot{U}_i^{(m)} + \frac{1}{2} \sum_{i=1}^3 \sum_{m=1}^2 \rho_{mm} \dot{U}_i^{(m)2} + T_L. \quad (26)$$

The LFF kinetic energy T_L in the FII and FCI cases are derived in the following section.

5 SPHERICAL HARMONICS AND LFF KINETIC ENERGY

Rayleigh analyzed the pressure in an incompressible liquid during the collapse of a spherical cavity (Rayleigh 1917). The whole kinetic energy of the liquid environment is given as an integral on thin liquid shells. Here, we extend Rayleigh's idea to a pocket-shell model, which includes kinetic energy of both the inner spherical pocket and surrounding fluid shell.

In the FII case, the kinetic energy of a single pocket Ω_1 (Fig. 4) and corresponding host medium is

$$T_{L-FII}^s = \frac{1}{2} \phi_{10} \int_{\Omega_1} \rho_{f_1} \dot{r}^2 d\Omega_1 + \frac{1}{2} \bar{\phi}_{20} \rho_{f_2} \int_{r_1}^{r_3} 4\pi r^2 \dot{r}^2 dr. \quad (27)$$

The first term represents the kinetic energy of the inner sphere $m = 1$. r_1, r_3 are the radii of the inner fluid pocket and outer fluid layer. $\bar{\phi}_{20}$ is the effective porosity of the outer fluid layer. In the triple-layer model, $\bar{\phi}_{20}$ is represented by $\bar{\phi}_{20} = \frac{\phi_{10}v_2 + \phi_{20}v_3}{v_2 + v_3}$, where v_2, v_3 are the volume fractions of layers 2 and 3, respectively and ϕ_{10}, ϕ_{20} are the porosities of the medium in layers 2 and 3 (Fig. 2a).

First, we calculate the integral in the inner domain Ω_1 . The fluid displacement r and velocity \dot{r} in T_{L-FII}^s are derived by spherical harmonics. In the fluid inside Ω_1 , the velocity is

$$\dot{\mathbf{r}} = \sum_{l,h} v_{lh}(t) r_{10} \nabla \left(\frac{r_0^l}{r_{10}^l} Y_l^h(\theta_0, \phi_0) \right), \quad (28)$$

where v_{lh} are time integrals of c_{lh} and $Y_l^h(\theta_0, \phi_0)$ are real spherical harmonics

$$v_{lh} = -\frac{1}{\rho_{f_1} r_{10}} \int c_{lh}(t) dt. \quad (29)$$

By time-integration of the velocity, we have the fluid displacement

$$\mathbf{r} = \mathbf{r}_0 + \sum_{l,h} r_{lh}(t) r_{10} \nabla \left[\frac{r_0^l}{r_{10}^l} Y_l^h(\theta_0, \phi_0) \right]. \quad (30)$$

The unperturbed fluid element position is \mathbf{r}_0 and position coefficients r_{lh} satisfy $\dot{r}_{lh} = v_{lh}$. In the case of irrotational vibrations, the displacement gradient is independent of θ_0, ϕ_0 and $\nabla = d/dr_0$. At the surface of phase zone $m = 1$, the radial displacement component is given by

$$r_1 = r_{10} + \sum_{l,h} r_{lh}(t) l Y_l^h(\theta_0, \phi_0). \quad (31)$$

The eigen functions $Y_l^h(\theta_0, \phi_0)$ are normalized to be orthonormal integrated over the surface of the unit sphere,

$$\frac{1}{4\pi} \int_{\theta_0=0}^{\pi} \int_{\phi_0=0}^{2\pi} Y_l^h(\theta_0, \phi_0) Y_{\bar{l}}^{\bar{h}}(\theta_0, \phi_0) \sin \theta_0 d\theta_0 d\phi_0 = \delta(l - \bar{l}) \delta(h - \bar{h}). \quad (32)$$

The final kinetic energy in phase zone $m = 1$ becomes

$$\frac{1}{2} \phi_{10} \int_{\Omega_1} \rho_{f_1} \dot{\mathbf{r}} \cdot \dot{\mathbf{r}} d\Omega_1 = \frac{1}{2} \phi_{10} \rho_{f_1} \sum_{l,h} \sum_{\bar{l},\bar{h}} \dot{r}_{lh} \dot{r}_{\bar{l}\bar{h}} r_1^3 \bar{l} \int_{\theta_0=0}^{\pi} \int_{\phi_0=0}^{2\pi} Y_l^h(\theta_0, \phi_0) Y_{\bar{l}}^{\bar{h}}(\theta_0, \phi_0) \sin \theta_0 d\theta_0 d\phi_0 = 2\pi \rho_{f_1} \phi_{10} r_1^3 \sum_{l,h} l \dot{r}_{lh}^2 \quad (33)$$

Considering the conservation of fluid flow between different internal surfaces, we have

$$4\pi r^2 \dot{r} \phi_{m0} = 4\pi r_1^2 \dot{r}_1 \phi_{10} = 4\pi r_2^2 \dot{r}_2 \phi_{20}, \quad \text{or} \quad \dot{r} = \frac{r_1^2 \dot{r}_1 \phi_{10}}{r^2 \phi_{m0}} = \frac{r_2^2 \dot{r}_2 \phi_{20}}{r^2 \phi_{m0}}, \quad (m = 1, 2, 3) \quad (34)$$

where \dot{r} is the radius of an arbitrary internal interface in phase m . For $l = h = 1$, the kinetic energy of the inner sphere is

$$\frac{1}{2} \phi_{10} \int_{\Omega_1} \rho_{f_1} \dot{\mathbf{r}} \cdot \dot{\mathbf{r}} d\Omega_1 = \frac{1}{2} \rho_{f_1} \phi_{10} r_1^3 \dot{r}_1^2. \quad (35)$$

Then kinetic energy related to TLP inclusion is written as

$$\begin{aligned} T_{L-FII}^s &= \frac{1}{2} \phi_{10} \int_{\Omega_1} \rho_{f_1} \dot{r}^2 d\Omega_1 + \frac{1}{2} \bar{\phi}_{20} \rho_{f_2} \int_{r_1}^{r_3} 4\pi r^2 \dot{r}^2 dr \\ &= 2\pi \rho_{f_1} \phi_{10} r_1^3 \dot{r}_1^2 + 2\pi \rho_{f_2} \frac{\phi_{10}^2}{\bar{\phi}_{20}} r_1^3 \dot{r}_1^2 \left[1 - \frac{r_1}{r_3} \right]. \end{aligned} \quad (36)$$

The first term in the above formula represents the kinetic energy of the inner inclusion, \dot{r}_{lh} is the fluid velocity caused by different components of the spherical harmonic vibrations at the surface of phase $m = 1$. The second term is related to the kinetic energy integral in the outer concentric shell domain. The relative fluid flow velocity approaches zero at infinite distance from the patchy center, therefore the boundary condition used here is the same as that of White (1975). If the surface of the inner fluid pocket is far from the outer boundary of the whole patch, that is if $r_1 \ll r_3$, the term r_1/r_3 can be neglected.

Considering the phase volume fraction relation $\phi_m = v_m \phi_{m0}$, we can write the volume ratio of the inclusion v_1 and layer v_3 as

$$v_1 = \frac{4}{3} \pi r_1^3 N_0 = \frac{\phi_1}{\phi_{10}} \quad \text{or} \quad r_1^3 = \frac{3\phi_1}{4\pi \phi_{10} N_0}. \quad (37)$$

Here, N_0 is the number of inclusions per unit volume of composite. Since $\dot{r}_1 \approx \frac{1}{3} r_{10} \phi_2 \dot{\zeta}$ has been derived in a previous section, we finally have the total LFF kinetic energy density $T_{L-FII} = N_0 T_{L-FII}^s$, expressed as

$$T_{L-FII} = \left(2\pi \rho_{f_1} \phi_{10} + 2\pi \rho_{f_2} \frac{\phi_{10}^2}{\bar{\phi}_{20}} \left(1 - \frac{r_1}{r_3} \right) \right) \frac{3\phi_1}{4\pi \phi_{10} N_0} \left(\frac{1}{3} r_{10} \bar{\phi}_2 \dot{\zeta} \right)^2 = \alpha_1 \frac{\phi_{10} \bar{\phi}_2^2}{6} r_{10}^2 \dot{\zeta}^2 \quad (38)$$

$$\alpha_1 = \left(\rho_{f_1} + \rho_{f_2} \frac{\phi_{10}}{\bar{\phi}_{20}} \left[1 - v_1^{1/3} \right] \right) v_1, \quad (39)$$

In the same way, the LFF kinetic energy density for the FCI case is

$$T_{L-FCI} = \alpha_2 \frac{\bar{\phi}_{10} \phi_2^2}{6} r_{20}^2 \dot{\zeta}^2 \quad (40)$$

$$\alpha_2 = \left[\rho_{f_1} + \rho_{f_2} \frac{\bar{\phi}_{10}}{\phi_{20}} \left(1 - (v_1 + v_2)^{1/3} \right) \right] (v_1 + v_2), \quad (41)$$

6 DISSIPATION FUNCTIONS

The dissipation includes both the Biot and mesoscopic loss mechanisms. Biot's dissipation is caused by the relative motion between the fluid and the frame. The dissipation function for the FII and FCI cases are (Biot 1962):

$$D_{\text{FII}} = \frac{1}{2} \left[v_1 b_1 \sum_{i=1}^3 \left(\dot{U}_i^{(1)} - \dot{u}_i \right)^2 + \bar{v}_2 \bar{b}_2 \sum_{i=1}^3 \left(\dot{U}_i^{(2)} - \dot{u}_i \right)^2 \right], \quad (42)$$

$$D_{\text{FCI}} = \frac{1}{2} \left[\bar{v}_1 \bar{b}_1 \sum_{i=1}^3 \left(\dot{U}_i^{(1)} - \dot{u}_i \right)^2 + v_3 b_3 \sum_{i=1}^3 \left(\dot{U}_i^{(2)} - \dot{u}_i \right)^2 \right], \quad (43)$$

$$b_1 = \phi_{10}^2 \frac{\eta_1}{\kappa_{10}}, \quad \bar{b}_2 = \bar{\phi}_{20}^2 \frac{\eta_2}{\bar{\kappa}_{20}}, \quad \bar{b}_1 = \bar{\phi}_{10}^2 \frac{\eta_1}{\bar{\kappa}_{10}}, \quad b_3 = \phi_{20}^2 \frac{\eta_2}{\kappa_{20}}, \quad (44)$$

$$\frac{1}{\bar{\kappa}_{10}} = \frac{v_1}{\kappa_{10} \bar{v}_1} + \frac{v_2}{\kappa_{20} \bar{v}_1}, \quad \frac{1}{\bar{\kappa}_{20}} = \frac{v_2}{\kappa_{10} \bar{v}_2} + \frac{v_3}{\kappa_{20} \bar{v}_2}. \quad (45)$$

The dissipation energy caused by the local fluid flow is derived in the same way as T_L .

$$\begin{aligned} D_{L-FII} &= \frac{1}{2} \phi_{10}^2 \frac{\eta_1}{\kappa_1} \int_{\Omega_1} 4\pi r^2 \dot{r}^2 d\Omega_1 + \frac{1}{2} \bar{\phi}_{20}^2 \frac{\eta_2}{\kappa_2} \int_{r_1}^{r_3} 4\pi r^2 \dot{r}^2 dr \\ &= \left(2\pi \frac{\eta_1}{\kappa_1} \phi_{10}^2 + 2\pi \frac{\eta_2}{\kappa_2} \bar{\phi}_{20}^2 [1 - v_1^{1/3}] \right) r_1^3 \dot{r}_1^2 = \beta_1 \frac{\phi_{10} \bar{\phi}_{20}^2}{6} r_{10}^2 \dot{\zeta}^2 \end{aligned} \quad (46)$$

$$\beta_1 = \left(\frac{\eta_1}{\kappa_{10}} + \frac{\eta_2}{\bar{\kappa}_{20}} (1 - v_1^{1/3}) \right) \phi_{10} v_1, \quad (47)$$

Similarly, the dissipation energy for the FCI case is

$$D_{L-FCI} = \beta_2 \frac{\bar{\phi}_{10} \phi_{20}^2}{6} r_{20}^2 \dot{\zeta}^2 \quad (48)$$

$$\beta_2 = \left(\frac{\eta_1}{\bar{\kappa}_{10}} + \frac{\eta_2}{\kappa_{20}} (1 - \bar{v}_1^{1/3}) \right) \bar{\phi}_{10} \bar{v}_1, \quad (49)$$

where $\eta_m, \kappa_m, (m = 1, 2, 3)$ are the viscosity and permeability in each layer.

7 WAVE PROPAGATION EQUATIONS

The dynamics of the entire porous system is determined by the Lagrangian function:

$$L = T - W, \quad (50)$$

where T is the total kinetic energy and W is the total potential energy. The Euler-Lagrange equation, containing dissipation function is

$$\frac{\partial}{\partial t} \left(\frac{\partial L}{\partial \dot{u}_i} \right) + \sum_{j=1}^3 \frac{\partial}{\partial x_j} \left(\frac{\partial L}{\partial u_{ij}} \right) + \frac{\partial L}{\partial u_i} + \frac{\partial (D + D_L)}{\partial \dot{u}_i} = 0. \quad (51)$$

where u_i represents the components of the solid displacement \mathbf{u} and the fluid displacement $\mathbf{U}^{(m)}$. Regarding the local fluid flow, the Euler-Lagrange equation is

$$\frac{\partial}{\partial t} \left(\frac{\partial L}{\partial \dot{\zeta}_m} \right) + \frac{\partial L}{\partial (\zeta_m)} + \frac{\partial (D + D_L)}{\partial \dot{\zeta}_m} = 0, \quad m = 1, 2. \quad (52)$$

Substituting T, W, D, D_L into the previous equations, the dynamic equations for the FII case are

$$N \nabla^2 \mathbf{u} + (A + N) \nabla I_1 + Q_1 \nabla (\xi_1 - \bar{\phi}_2 \zeta) + \bar{Q}_2 \nabla (\xi_2 + \phi_1 \zeta) = \rho_{00} \ddot{\mathbf{u}} + \sum_{m=1}^2 [\rho_{0m} \ddot{\mathbf{U}}^{(m)} + b_m (\dot{\mathbf{u}} - \dot{\mathbf{U}}^{(m)})], \quad (53)$$

$$Q_1 \nabla I_1 + R_1 \nabla (\xi_1 - \bar{\phi}_2 \zeta) = \rho_{01} \ddot{\mathbf{u}} + \rho_{11} \ddot{\mathbf{U}}^{(1)} + b_1 (\dot{\mathbf{U}}^{(1)} - \dot{\mathbf{u}}), \quad (54)$$

$$\bar{Q}_2 \nabla I_1 + \bar{R}_2 \nabla (\xi_2 + \phi_1 \zeta) = \rho_{02} \ddot{\mathbf{u}} + \rho_{22} \ddot{\mathbf{U}}^{(2)} + \bar{b}_2 (\dot{\mathbf{U}}^{(2)} - \dot{\mathbf{u}}), \quad (55)$$

$$\bar{\phi}_2 Q_1 I_1 + \bar{\phi}_2 R_1 (\xi_1 - \bar{\phi}_2 \zeta) - \phi_1 \bar{Q}_2 I_1 - \phi_1 \bar{R}_2 (\xi_2 + \phi_1 \zeta) = -(\alpha_1 \ddot{\zeta} + \beta_1 \dot{\zeta}) \frac{\phi_{10} \bar{\phi}_{20}^2}{3} r_{10}^2, \quad (56)$$

The porous system of TLP model has ten unknowns $\{u_i, U_i^{(m)}, \zeta\}$, $i = 1, 2, 3, m = 1, 2, 3$, which can be determined from the previous equations.

The dynamical equations for the FCI case are derived in the same way as the FII ones. The only difference is that the inner and middle layers are merged into an effective sphere. The porosity and coefficients in the FCI case are $\bar{\phi}_1, \bar{R}_1, \bar{Q}_1, \bar{b}_1$. While the outer layer contains different fluid with parameters ϕ_1, R_2, Q_2, b_2 . The dynamical equations are

$$N\nabla^2 \mathbf{u} + (A + N)\nabla I_1 + \bar{Q}_1 \nabla (\xi_1 - \phi_2 \zeta) + Q_2 \nabla (\xi_2 + \bar{\phi}_1 \zeta) = \rho_{00} \ddot{\mathbf{u}} + \sum_{m=1}^2 [\rho_{0m} \ddot{\mathbf{U}}^{(m)} + b_m (\dot{\mathbf{u}} - \dot{\mathbf{U}}^{(m)})], \quad (57)$$

$$\bar{Q}_1 \nabla I_1 + \bar{R}_1 \nabla (\xi_1 - \phi_2 \zeta) = \rho_{01} \ddot{\mathbf{u}} + \rho_{11} \ddot{\mathbf{U}}^{(1)} + \bar{b}_1 (\dot{\mathbf{U}}^{(1)} - \dot{\mathbf{u}}), \quad (58)$$

$$Q_2 \nabla I_1 + R_2 \nabla (\xi_2 + \bar{\phi}_1 \zeta) = \rho_{02} \ddot{\mathbf{u}} + \rho_{22} \ddot{\mathbf{U}}^{(2)} + b_2 (\dot{\mathbf{U}}^{(2)} - \dot{\mathbf{u}}), \quad (59)$$

$$\phi_2 \bar{Q}_1 I_1 + \phi_2 \bar{R}_1 (\xi_1 - \phi_2 \zeta) - \bar{\phi}_1 Q_2 I_1 - \bar{\phi}_1 R_2 (\xi_2 + \bar{\phi}_1 \zeta) = -(\alpha_1 \ddot{\zeta} + \beta_1 \dot{\zeta}) \frac{\bar{\phi}_{10} \phi_2^2}{3} r_{10}^2. \quad (60)$$

8 PLANE-WAVE ANALYSIS

Assuming that the porous medium is homogeneous and isotropic, we obtain the plane-wave propagation. The wave kernel $e^{i(\omega t - \mathbf{k} \cdot \mathbf{x})}$ is used in the derivations, where ω is the angular frequency and \mathbf{k} is the vector wavenumber. Substituting the plane-wave kernel into the dynamical equations, we obtain

$$\nabla^2 \mathbf{u} = -k^2 \mathbf{u}, \quad \dot{\mathbf{u}} = i\omega \mathbf{u}, \quad \ddot{\mathbf{u}} = -\omega^2 \mathbf{u}, \quad (61)$$

$$\dot{\mathbf{U}}^{(m)} = i\omega \mathbf{U}^{(m)}, \quad \ddot{\mathbf{U}}^{(m)} = -\omega^2 \mathbf{U}^{(m)}, \quad (62)$$

$$I_1 = \nabla \cdot \mathbf{u} = i\nabla(-\mathbf{k} \cdot \mathbf{x}) \cdot \mathbf{u}, \quad \nabla I_1 = -k^2 \mathbf{u}, \quad (63)$$

$$\xi_m = \nabla \cdot \mathbf{U}^{(m)} = i\nabla(-\mathbf{k} \cdot \mathbf{x}) \cdot \mathbf{U}^{(m)}, \quad \nabla \xi_m = -k^2 \mathbf{U}^{(m)}, \quad (64)$$

$$\zeta = \nabla \cdot \mathbf{Z} = i\nabla(-\mathbf{k} \cdot \mathbf{x}) \cdot \mathbf{Z}, \quad \nabla \zeta = -k^2 \mathbf{Z}, \quad (65)$$

$$\dot{\zeta} = i\omega \cdot i\nabla(-\mathbf{k} \cdot \mathbf{x}) \cdot \mathbf{Z}, \quad \ddot{\zeta} = -\omega^2 \cdot i\nabla(-\mathbf{k} \cdot \mathbf{x}) \cdot \mathbf{Z}. \quad (66)$$

Then, we get the dynamic equations for the FII and FCI cases as

$$\begin{bmatrix} (A + 2N)k^2 - \rho_{00}\omega^2 + i\omega(b_1 + \bar{b}_2) & (Q_1 k^2 - \rho_{01}\omega^2 - i\omega b_1) & (\bar{Q}_2 k^2 - \rho_{02}\omega^2 - i\omega \bar{b}_2) & (\bar{Q}_2 \phi_1 - Q_1 \bar{\phi}_2) k^2 \\ (Q_1 k^2 - \rho_{01}\omega^2 - i\omega b_1) & (R_1 k^2 - \rho_{11}\omega^2 + i\omega \bar{b}_1) & 0 & -R_1 \bar{\phi}_2 k^2 \\ (Q_2 k^2 - \rho_{02}\omega^2 - i\omega \bar{b}_2) & 0 & (\bar{R}_2 k^2 - \rho_{22}\omega^2 + i\omega \bar{b}_2) & \bar{R}_2 \phi_1 k^2 \\ (\bar{Q}_2 \phi_1 - Q_1 \bar{\phi}_2) k^2 & -R_1 \bar{\phi}_2 k^2 & \bar{R}_2 \phi_1 k^2 & [\bar{\phi}_2^2 R_1 + \phi_1^2 \bar{R}_2 - \frac{\phi_{10} \bar{\phi}_2^2 \omega}{3} r_{10}^2 (-\alpha_1 \omega + i\beta_1)] k^2 \end{bmatrix} \times \begin{bmatrix} u_i \\ U_i^{(1)} \\ U_i^{(2)} \\ Z_i \end{bmatrix} = 0, \quad (i = 1, 2, 3) \quad (67)$$

$$\begin{bmatrix} (A + 2N)k^2 - \rho_{00}\omega^2 + i\omega(\bar{b}_1 + b_2) & (\bar{Q}_1 k^2 - \rho_{01}\omega^2 - i\omega \bar{b}_1) & (Q_2 k^2 - \rho_{02}\omega^2 - i\omega b_2) & (Q_2 \bar{\phi}_1 - \bar{Q}_1 \phi_2) k^2 \\ (\bar{Q}_1 k^2 - \rho_{01}\omega^2 - i\omega \bar{b}_1) & (\bar{R}_1 k^2 - \rho_{11}\omega^2 + i\omega \bar{b}_1) & 0 & -\bar{R}_1 \phi_2 k^2 \\ (Q_2 k^2 - \rho_{02}\omega^2 - i\omega b_2) & 0 & (R_2 k^2 - \rho_{22}\omega^2 + i\omega b_2) & R_2 \bar{\phi}_1 k^2 \\ (Q_2 \bar{\phi}_1 - \bar{Q}_1 \phi_2) k^2 & -\bar{R}_1 \phi_2 k^2 & R_2 \bar{\phi}_1 k^2 & [\phi_2^2 \bar{R}_1 + \bar{\phi}_1^2 R_2 - \frac{\phi_{10} \phi_2^2 \omega}{3} r_{20}^2 (-\alpha_2 \omega + i\beta_2)] k^2 \end{bmatrix} \times \begin{bmatrix} u_i \\ U_i^{(1)} \\ U_i^{(2)} \\ Z_i \end{bmatrix} = 0, \quad (i = 1, 2, 3) \quad (68)$$

Table 1. French Vosgian sandstone properties.

Property	
ϕ	0.21
K_s (GPa)	37
ρ_s (kg m ⁻³)	2650
V_p (m s ⁻¹)	2050
V_s (m s ⁻¹)	1240
κ (m ²)	1.1×10^{-13}
$V_{p\text{water}}$ (m s ⁻¹)	1550
ρ_{water} (kg m ⁻³)	1015
η_{water} (Pa s)	0.001
$V_{p\text{oil}}$ (m s ⁻¹)	1275
ρ_{oil} (kg m ⁻³)	755
η_{gas} (Pa s)	0.076

The relationship between the wavenumber k and the frequency ω can be obtained by setting the determinant of the dynamical equations to zero, that is,

$$\begin{vmatrix} a_{11}k^2 + b_{11} & a_{12}k^2 + b_{12} & a_{13}k^2 + b_{13} \\ a_{21}k^2 + b_{21} & a_{22}k^2 + b_{22} & a_{23}k^2 + b_{23} \\ a_{31}k^2 + b_{31} & a_{32}k^2 + b_{32} & a_{33}k^2 + b_{33} \end{vmatrix} = 0, \quad (69)$$

These equations in k^2 have three roots, corresponding to the fast P wave and two slow P waves. Here, the coefficients a_{ij}, b_{ij} ($i = 1, 2, 3, j = 1, 2, 3$) are functions of frequency ω , porosity ϕ , the stiffnesses and the density coefficients (see Appendix B). The complex and phase P -wave velocities are defined as

$$v = \frac{\omega}{k}, \quad (70)$$

$$v_P = \text{Re}(v), \quad (71)$$

respectively. The P -wave dissipation factor is

$$Q^{-1} = \frac{\text{Im}(v^2)}{\text{Re}(v^2)}. \quad (72)$$

9 NUMERICAL EXAMPLES

9.1 Laboratory data comparison for the oil-brine saturated sandstone

In the first example, we obtain the P -wave velocity in French Vosgian sandstone, which is saturated with oil and brine with an average porosity of 21 per cent. Table 1 shows the rock properties reported by Bacri & Salin (1986). The partial oil/brine saturations are achieved by imbibition and drainage methods. Here, the frequency at which the acoustic velocities were measured is 350 kHz.

The P -wave dispersion/attenuation curves are computed with the White, Johnson, Biot–Rayleigh (BR) and TLP models, respectively. In addition, the BGW and BGH limits are calculated as velocity bounds. We consider two special cases of the TLP model. (1) The TLP model reduces to a single-porosity/dual-fluid model by setting the solid inclusion radius to zero or whole patch size. The effect of the inner fluid pocket kinetic energy is excluded. The data is tagged as $TLP^{R_{si}=0}$ or $TLP^{R_{si}=R_{patch}}$. (2) The effect of the inner fluid pocket kinetic energy is included, with the TLP model reducing to the single-porosity/dual-fluid model by setting the solid inclusion radius to zero. The data is tagged as $TLP_{inner}^{R_{si}=0}$.

When the TLP model is reduced to single-porosity/dual-fluid case, the whole region has a unique type of rock matrix. It is straightforward to show that the equations of the cases FII and FCI are the same. Figs 5 and 6 show that the P -wave dispersion/attenuation curves corresponding to the $R_{si} = 0$ and $R_{si} = R_{patch}$ cases overlap.

The difference between the case with $TLP^{R_{si}=0}$ and the case with $TLP_{inner}^{R_{si}=0}$ is non-negligible (Fig. 5). In the first case the radius of the inner spherical matrix with porosity ϕ_{in} is set to zero and the kinetic energy of the inner fluid pocket is neglected. Thus, the double-porosity dual-fluid model reduces to the traditional single-porosity dual-fluid model. In the second case the kinetic energy of the inner fluid pocket is included. These differences in the velocity dispersion curves (Fig. 5) are due to the inner fluid pocket. The local fluid flow kinetic energy of the inner fluid pocket is included when deriving the equations of the TLP model (the first integral term in eq. 27, as well as the one in eq. 36).

The TLP model provides a method to predict dispersion and attenuation caused by both fluid and solid heterogeneities. The curves are different from the White and Johnson results. The local fluid flow kinetic energy T_L of the inner fluid pocket is included in deriving the equations of TLP model, which lead to an extra term ρ_{f_1} in the coefficient $\alpha_1 = (\rho_{f_1} + \rho_{f_2} \frac{\phi_{10}}{\phi_{20}})$. However, the BR model ignores the inner gas

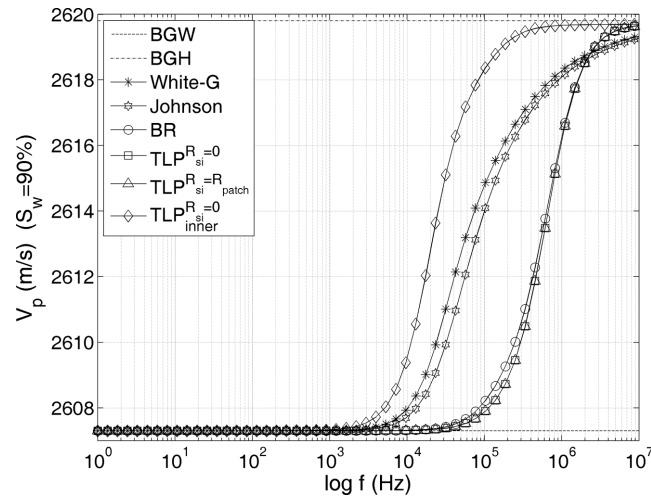


Figure 5. *P*-wave phase velocity as a function of frequency, corresponding to the different models. Water saturation is 90 per cent and the inner fluid pocket (oil droplet) radius is $R_a = 1$ mm. The TLP model reduces to the double-porosity model by setting the inclusion radius $R_{si} = 0$.

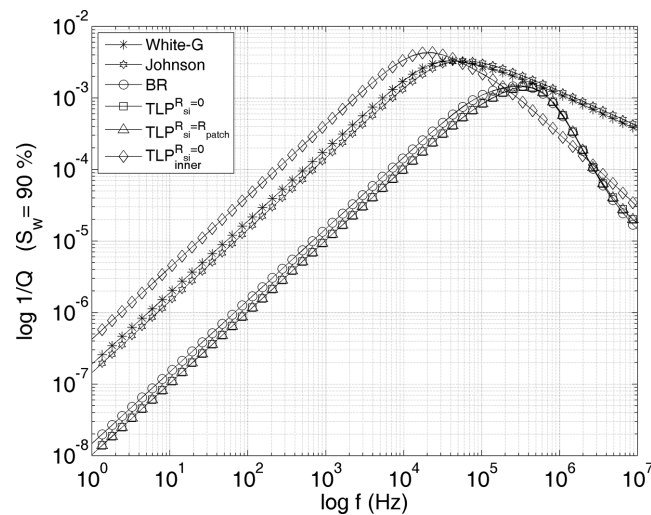


Figure 6. *P*-wave attenuation as a function of frequency, corresponding to the different models. Water saturation is 90 per cent and the inner fluid pocket radius (oil droplet) is $R_a = 1$ mm. The TLP model reduces to the double-porosity model by setting inclusion radius $R_{si} = 0$.

pocket energy. Differences between the predicted TLP and BR velocities are relatively small compared with the total velocity range for water saturations from 0 to 100 per cent. The TLP model results considering the inner fluid kinetic energy are close to those of the BR model (see Fig. 7), indicating that the velocity difference caused by the inner fluid pocket is about 0.7 per cent at most.

9.2 Velocity prediction for the high porosity sandstone at sonic frequency

The next example corresponds to a North-Sea sandstone with a porosity of 35 per cent and permeability of 8.7D. The rock and fluid properties are reported by Boruah & Chatterjee (2010) are given in Table 2.

The frame bulk moduli K_b and N are calculated by using Pride's equations $K_b = \frac{K_s(1-\phi)}{1+\alpha\phi}$ and $N = \frac{N_s(1-\phi)}{1+1.5\alpha\phi}$ (Pride & Berryman 2003a,b). The consolidation parameter α is determined by fitting the dry-frame velocity of the North-Sea sandstones. The velocities of the North-Sea sandstone as a function of brine saturation are given in Batzle *et al.* (2006).

The photomicrographs show that the mean grain size of the North-Sea sandstone is about 100 μm (Avseth 2000). The presence of clay increases the pore surface to volume ratio. The water adsorption weakens the frame moduli and significant velocity dispersion/attenuation occurs in the sandstone. The acoustic phase velocities have been reported as a function of brine saturation at the seismic, sonic and ultrasonic frequency ranges (Batzle *et al.* 2006). The sample has high porosity and the saturation is heterogeneous.

Here, the complete TLP model is applied to the North-Sea sandstone, that is double-porosity and dual-fluid are assumed. The sandstone is predominantly composed of quartz with clay coating the mineral grains (Avseth 2000). The clay and organic matter coating the sand grains tend to inhibit quartz cementation. The clay content in the pore system leads to a great number of small size contact gaps. The losses are therefore greater because of the higher number of dissipation mechanisms.

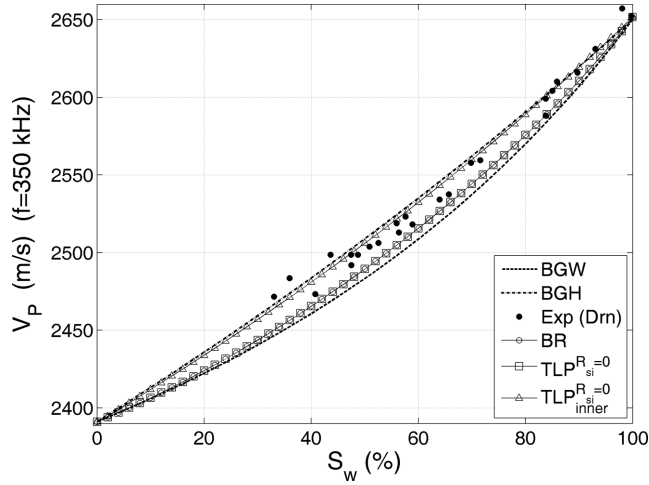


Figure 7. *P*-wave velocity as a function of water saturation, corresponding to the BR and TLP models. Wave frequency is 350 kHz and the inner fluid pocket radius (oil droplet) is $R_a = 1$ mm. The TLP model reduces to the double-porosity model by setting the inclusion radius $R_{si} = 0$. The experimental data is shown.

Table 2. Rock and fluid parameters for North Sea sandstone.

Property	Value
ϕ	0.35
K_s (GPa)	39.47
ρ_s (kg m^{-3})	2630
N (GPa)	36.61
κ (m^2)	8.586×10^{-12}
K_{brine} (GPa)	2.48
ρ_{brine} (kg m^{-3})	1060
η_{brine} (Pa s)	0.0011
K_{gas} (GPa)	1.01×10^{-5}
ρ_{gas} (kg m^{-3})	1.2
η_{gas} (Pa s)	1.81×10^{-5}

Since the velocity dispersion is caused by the local fluid flow between inclusions and host media, the ratio between the diffusion length and the mesoscopic fluid patch size is important. When the wave frequency is sufficiently low, the characteristic patch size of the fluid heterogeneities is much smaller than the diffusion length. Since the fluids have enough time to relax, Wood’s law is applied to calculate an effective fluid bulk modulus in the form of the harmonic saturation-weighted average of the individual fluid bulk moduli (Gassmann–Wood limit). On the contrary, when the wave frequency is sufficiently high and the characteristic patch size is larger than the diffusion length, the fluid-flow relaxation effects can be ignored. The diffusion length in a porous rock can be determined by $\lambda_p = \sqrt{\frac{\kappa M L}{\omega \eta H}}$, with L, H being the *P*-wave moduli of the dry and fluid-saturated rock. Here $M = [(\alpha - \phi)/K_s + \phi/K_f]^{-1}$ and $\alpha = 1 - K_b/K_s$, with κ, η denoting flow permeability and viscosity, respectively.

The ratio of the volume of the water patch to the bounding area (V/A) has been used as a measure of patch size. The theory of acoustics of patchy-saturation (APS) is proposed to deduce the value of V/A from experimental data on wave velocity and attenuation in partially water-saturated limestones (Tserkovnyak & Johnson 2002). The patch size is found as a function of the fractional water-saturation. Tserkovnyak & Johnson (2002) reported that the APS theory does not work in the case of high and low permeability samples. Some of the deduced V/A values exceed the expected limits at high saturation $S > 0.99$. They ascribed the failure to the neglected capillary effects or heterogeneities in permeability.

In this example, the sandstone has a high permeability. We determine the patch size by estimating the diffusion length λ_p at the low frequency band. The effective fluid bulk modulus K_f at different saturations is calculated as the harmonic saturation-weighted average of the individual fluid bulk moduli. The wave frequencies are so low that the characteristic patch size is much smaller than the diffusion length. The patch size is defined as $R = a\lambda_p$ with a small coefficient a . Calculations show that $a = 0.2$ will give a satisfactory fit to the experiment data at the seismic frequency (Fig. 8). The patch sizes approximately range from 0.3 to 2.3 cm for water saturations from 0 to 1. The estimated patch size range is consistent with those determined from velocities and attenuation in partially water saturated limestone (Tserkovnyak & Johnson 2002). The photomicrographs show that the mean grain size of the North-Sea sandstone is 100 μm (Avseth 2000). Thus, the patch is roughly 30–230 times the grain size. The volume fraction of the outer sphere is chosen to be 80 per cent. In the outer sphere, the porosity is 65 per cent of the main matrix porosity and the grain density is 85 per cent of the frame grain density. With these values, ϕ_{20} is approximately 0.23 and ρ_{01} is 2236 kg m^{-3} . All the other parameters are listed in Table 2.

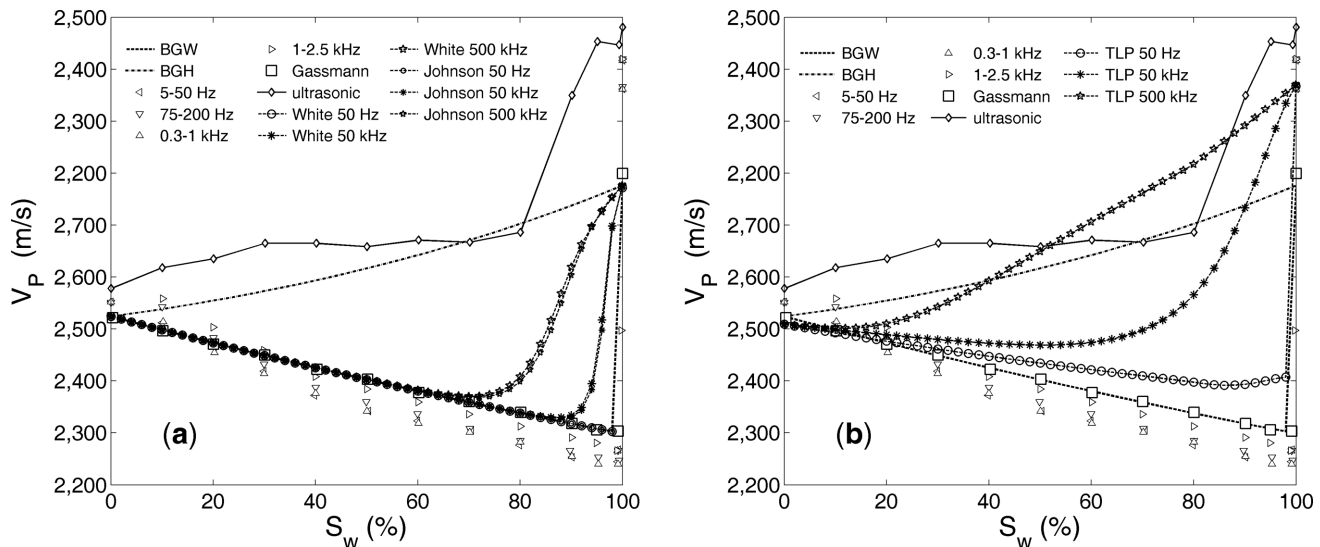


Figure 8. Measured and theoretically predicted P -wave velocities for the North-Sea sandstone. The symbols of 5–50 Hz, 75–200 Hz, 0.3–1 kHz and 1–2.5 kHz and ultrasonic wave are experimental data following Batzle *et al.* (2006). (a) Predictions of White and Johnson models, (b) predictions of TLP model.

Having the patch size and inclusion volume fraction, we calculated the P -wave dispersion and attenuation for North-Sea sandstone. The P -wave velocities at different water saturation are computed with the TLP, generalized White and Johnson models and shown in Fig. 8. The results of the generalized White and Johnson models are bounded by the BGW and BGH limits. Although the predictions of the TLP model are not perfect, the predicted 500 kHz curve is able to approach the experimentally-measured data which are outside the range of the BGW and BGH limits. By introducing locally different porosities, the TLP model fits experimental data which cannot be predicted with conventional patch models. However, as it is shown in Fig. 8, all the models can hardly predict the noticeably higher ultrasonic wave velocity at low saturations (<50 per cent). The difference has been ascribed to sample heterogeneity (Batzle *et al.* 2006), where a combined effect of the fluid flows from different heterogeneities may affect the wave propagation.

10 CONCLUSIONS

A new mesoscopic-loss model has been derived to investigate the compressional-wave dissipation process in a double-porosity/dual-fluid medium. The significance of this work is to combine both mesoscopic-scale heterogeneities in the porous skeleton and the pore fluid saturation in a triple-layer geometry. The three solid-fluid heterogeneity combinations are achieved by assigning different rock and fluid properties to each layer. The model is based on Biot theory and Lagrange equations, which incorporate both the Biot and local-flow attenuation mechanisms. A detailed comparison between the predictions of the model and measurements of wave velocity and attenuation are given, as well as comparisons to the White, Johnson and BR models. The agreement among the different models is reasonably good in the case of particular version of the new model. The TLP model considers the inner fluid kinetic energy and there is slightly small differences between the predicted TLP and BR velocities for water saturations from 0 to 100 per cent. Although all the models predict attenuation and velocity dispersion typical of a relaxation process, there are differences. Application of the models to a North-Sea sandstone, from seismic to ultrasonic frequencies, suggests that the incorporation of heterogeneities in the matrix improves the prediction of the P -wave velocity approaching full saturation.

ACKNOWLEDGEMENTS

This research was sponsored by the National Natural Science Foundation of China (41390454) and the Foundation of State Key Laboratory of Petroleum Resources and Prospecting, China University of Petroleum, Beijing (No. PRP/open-1511).

REFERENCES

- Arntsen, B. & Carcione, J.M., 2001. Numerical simulation of the Biot slow wave in water-saturated Nivelsteiner Sandstone, *Geophysics*, **66**, 890–896.
- Avseth, P., 2000. Combining rock physics and sedimentology for seismic reservoir characterization of North Sea turbidite systems, *Degree of Doctor of Philosophy*, Stanford University.
- Ba, J., Carcione, J.M. & Nie, J.X., 2011. Biot-Rayleigh theory of wave propagation in double-porosity media, *J. geophys. Res.*, **116**, B06202, doi:10.1029/2010JB008185.
- Ba, J., Carcione, J.M. & Sun, W.T., 2015. Seismic attenuation due to heterogeneities of rock fabric and fluid distribution, *Geophys. J. Int.*, **202**(3), 1843–1847.
- Bacri, J.-C. & Salin, D., 1986. Sound velocity of a sandstone with oil and brine at different concentrations, *Geophys. Res. Lett.*, **13**, 326–328.
- Batzle, M.L., Han, D.H. & Hofmann, R., 2006. Fluid mobility and frequency-dependent seismic velocity - direct measurements, *Geophysics*, **71**, N1–N9.
- Berryman, J.G. & Wang, H.F., 1995. The elastic coefficients of double-porosity models for fluid transport in jointed rock, *J. geophys. Res.: Solid Earth*, **100**, 24 611–24 627.

- Berryman, J.G. & Wang, H.F., 2000. Elastic wave propagation and attenuation in a double-porosity dual-permeability medium, *Int. J. Rock. Mech. Min.*, **37**, 63–78.
- Biot, M.A., 1956a. Theory of propagation of elastic waves in a fluid-saturated porous solid. 1. Low-frequency range, *J. acoust. Soc. Am.*, **28**, 168–178.
- Biot, M.A., 1956b. Theory of propagation of elastic waves in a fluid-saturated porous solid. 2. Higher frequency range, *J. acoust. Soc. Am.*, **28**, 179–191.
- Biot, M.A., 1962. Mechanics of deformation and acoustic propagation in porous media, *J. appl. Phys.*, **33**, 1482–1498.
- Boruah, N. & Chatterjee, R., 2010. Rock physics template (RPT) analysis of well logs and seismic data for lithology and fluid classification, *Petroview*, **3**, 13–27.
- Carcione, J.M., 2015. *Wave Fields in Real Media: Wave Propagation in Anisotropic, Anelastic, Porous and Electromagnetic Media*, 3rd edn, Elsevier Science.
- Carcione, J.M. & Picotti, S., 2006. P-wave seismic attenuation by slow-wave diffusion: effects of inhomogeneous rock properties, *Geophysics*, **71**, O1–O8.
- Dutta, N.C. & Odé, H., 1979a. Attenuation and dispersion of compressional waves in fluid-filled porous rocks with partial gas saturation (White model). 1. Biot theory, *Geophysics*, **44**, 1777–1788.
- Dutta, N.C. & Odé, H., 1979b. Attenuation and dispersion of compressional waves in fluid-filled porous rocks with partial gas saturation (White model). 2. Results, *Geophysics*, **44**, 1789–1805.
- Dutta, N.C. & Seriff, A.J., 1979. On White's model of attenuation in rocks with partial gas saturation, *Geophysics*, **44**, 1806–1812.
- Dvorkin, J., Mavko, G. & Nur, A., 1995. Squirt flow in fully saturated rocks, *Geophysics*, **60**, 97–107.
- Johnson, D.L., 2001. Theory of frequency dependent acoustics in patchy-saturated porous media, *J. acoust. Soc. Am.*, **110**, 682–694.
- Mavko, G.M. & Nur, A., 1979. Wave attenuation in partially saturated rocks, *Geophysics*, **44**, 161–178.
- Mochizuki, S., 1982. Attenuation in partially saturated rocks, *J. geophys. Res.*, **87**, 8598–8604.
- Nur, A., 1971. Viscous phase in rocks and low-velocity zone, *J. geophys. Res.*, **76**, 1270–1277.
- Nur, A., 1973. Role of pore fluids in faulting, *Phil. Trans. R. Soc. Lond., A.*, **274**, 297–304.
- Oconnell, R.J. & Budiansky, B., 1977. Viscoelastic properties of fluid-saturated cracked solids, *J. geophys. Res.*, **82**, 5719–5735.
- Pride, S.R. & Berryman, J.G., 2003a. Linear dynamics of double-porosity dual-permeability materials. I. Governing equations and acoustic attenuation, *Phys. Rev. E*, **68**, doi:10.1103/PhysRevE.68.036603.
- Pride, S.R. & Berryman, J.G., 2003b. Linear dynamics of double-porosity dual-permeability materials. II. Fluid transport equations, *Phys. Rev. E*, **68**, doi:10.1103/PhysRevE.68.036604.
- Pride, S.R., Berryman, J.G. & Harris, J.M., 2004. Seismic attenuation due to wave-induced flow, *J. geophys. Res.*, **109**, B01201, doi:10.1029/2003JB002639.
- Quan, Y.L. & Harris, J.M., 1997. Seismic attenuation tomography using the frequency shift method, *Geophysics*, **62**, 895–905.
- Quintal, B., Steeb, H., Frehner, M. & Schmalholz, S.M., 2011. Quasi-static finite element modeling of seismic attenuation and dispersion due to wave-induced fluid flow in poroelastic media, *J. geophys. Res.: Solid Earth*, **116**, B01201, doi:10.1029/2010JB007475.
- Rayleigh, L., 1917. On the pressure developed in a liquid during the collapse of a spherical cavity, *Phil. Mag.*, **34**, 94–98.
- Rubino, J.G. & Holliger, K., 2012. Seismic attenuation and velocity dispersion in heterogeneous partially saturated porous rocks, *Geophys. J. Int.*, **188**, 1088–1102.
- Sams, M.S., Neep, J.P., Worthington, M.H. & King, M.S., 1997. The measurement of velocity dispersion and frequency-dependent intrinsic attenuation in sedimentary rocks, *Geophysics*, **62**, 1456–1464.
- Solomon, S.C., 1972. Seismic-wave attenuation and partial melting in upper mantle of North-America, *J. geophys. Res.*, **77**, 1483–1502.
- Thas, K., 2007. Can one hear the shape of a Lie-type geometry, *Inverse Probl.*, **23**, 2021–2028.
- Tserkovnyak, Y. & Johnson, D.L., 2002. Can one hear the shape of a saturation patch, *Geophys. Res. Lett.*, **29**, doi:10.1029/2001GL014709.
- White, J.E., 1975. Computed seismic speeds and attenuation in rocks with partial gas saturation, *Geophysics*, **40**, 224–232.
- White, J.E., Mikhaylova, N.G. & Lyakhovitskiy, F.M., 1975. Low-frequency seismic waves in fluid-saturated layered rocks, *J. acoust. Soc. Am.*, **57**, 654–659.

APPENDIX: STIFFNESS AND DENSITY COEFFICIENTS

Considering the general form of the strain energy, we derive the stress components as

$$\tau_{ij} = \frac{\partial W}{\partial e_{ij}} = \left(AI_1 + \sum_{m=1}^2 Q_m \xi_m \right) \delta_{ij} + 2N e_{ij} \quad (\text{A1})$$

$$\tau^{(m)} = \frac{\partial W}{\partial \xi_m} = Q_m I_1 + R_m \xi_m, \quad (\text{A2})$$

where $\frac{\partial I_1}{\partial e_{ij}} = \delta_{ij}$, $\frac{\partial I_2}{\partial e_{ij}} = I_1 \delta_{ij} - e_{ij}$ are used in the derivation. Following gedanken experiments, we derived the stiffness coefficients.

Case 1: In the pure shear deformation case, $I_1 = \xi_m = 0$. The solid stress becomes $\tau^{(m)} = 0$ and

$$\tau_{ij} = 2N e_{ij} = 2\mu_b e_{ij}. \quad (\text{A3})$$

Here $N = \mu_b$ is the dry-rock shear modulus.

Case 2: Assuming that there is a flexible rubber jacket surrounding the rock sample, we come to the second case. The pore fluid is unloaded ($\tau^{(m)} = 0$) and allowed to flow in and out. Then we have $\xi_m = -(Q_m I_1)/R_m$.

The skeleton is subjected to a hydrostatic pressure p_0 and $I_1 = \nabla \cdot \mathbf{u} = -p_0/K_b$, where K_b is the frame modulus. Substituting $\tau_{ij} = -p_0$, ξ_m and I_1 into stress equation, we have

$$A + \frac{2}{3}N - \sum_{m=1}^2 \frac{Q_m^2}{R_m} = K_b \quad (\text{A4})$$

Case 3: The rock sample is subjected to a uniform hydrostatic pressure p_1 . The mineral grain is homogeneous and isotropic. Then we have $\tau_{ij} = -(1 - \sum_{m=1}^2 \phi_m) p_1 \delta_{ij}$, $\tau^{(m)} = -\phi_m p_1$, $I_1 = -p_1/K_s$ and $\xi_m = -p_1/K_{f_m}$, where K_s, K_{f_m} are the solid and fluid bulk moduli.

Here, we neglect the LFF process. Substituting the above equations into τ^{ij} , $\tau^{(m)}$, we get

$$\frac{A + \frac{2}{3}N}{K_s} + \sum_{m=1}^2 \frac{Q_m}{K_{f_m}} = 1 - \sum_{m=1}^2 \phi_m, \quad (\text{A5})$$

$$\frac{Q_m}{K_s} + \frac{R_m}{K_{f_m}} = \phi_m, \quad m = 1, 2. \quad (\text{A6})$$

Case 4: In the case of an unloaded pore fluid ($\tau^{(m)} = 0$), we have $\xi_m = -Q_m I_1 / R_m$. If each single phase is isolated from the others, the elastic constants given by the single-porosity Biot's theory satisfy $Q_{m0} I_1^{(m)} + R_{m0} \xi_m = 0$, that is, $Q_{m0} / R_{m0} = \alpha_m / \phi_{m0} - 1$, where $\alpha_m = 1 - K_{bm} / K_{sm}$ is the Biot-Willis coefficient (Berryman & Wang 2000). Then, we define $\beta_{12} \equiv \frac{\xi_1}{\xi_2} = \frac{Q_1 R_2}{Q_2 R_1} \approx \frac{Q_{10} R_{20} I_1^{(1)}}{Q_{20} R_{10} I_1^{(2)}}$.

Considering that $I_1^{(m)} = -p_0 / K_{bm}$, Q_m, R_m satisfy

$$\frac{Q_1 R_2}{Q_2 R_1} = \frac{\phi_{20}}{\phi_{10}} \left[\frac{1 - (1 - \phi_{10}) K_{sm} / K_{b1}}{1 - (1 - \phi_{20}) K_{sm} / K_{b2}} \right] \equiv \frac{1}{\beta} \quad (\text{A7})$$

Since we have six unknowns $A, N, Q_m, R_m, m = 1, 2$ and six equations, the stiffness can be determined as follows

$$A = \left(1 - \sum_{m=1}^2 \phi_m \right) K_s - \frac{2}{3}N - K_s \sum_{m=1}^2 \frac{Q_m}{K_{f_m}}, \quad (\text{A8})$$

$$Q_m = \frac{K_s \phi_m}{1 + \gamma_m}, \quad (\text{A9})$$

$$R_m = \frac{K_{f_m} \phi_m}{1 + 1/\gamma_m}, \quad m = 1, 2, \quad (\text{A10})$$

$$\gamma_1 = \frac{K_s}{K_{f_1}} \left[\frac{\phi_1 + \phi_2 \beta}{1 - K_b / K_s - \sum_{m=1}^2 \phi_m} \right], \quad (\text{A11})$$

$$\gamma_2 = \frac{K_s}{\beta K_{f_2}} \left[\frac{\phi_1 + \phi_2 \beta}{1 - K_b / K_s - \sum_{m=1}^2 \phi_m} \right], \quad (\text{A12})$$

For the FII case, the coefficients for phase $m = 2$ are \bar{Q}_2, \bar{R}_2 and the porosities ϕ_2, ϕ_{20} are replaced by $\bar{\phi}_2, \bar{\phi}_{20}$. For the FCI case, the coefficients for phase $m = 1$ are \bar{Q}_1, \bar{R}_1 and ϕ_1, ϕ_{10} are replaced by $\bar{\phi}_1, \bar{\phi}_{10}$.

Following the calculations of the density coefficients proposed by Biot, we derive the expressions for $\rho_{00}, \rho_{0m}, \rho_{mm}$. Assuming that there is no relative motion between the fluid and solid, we have $u_i = U_i^{(m)}$. The pressure difference in the fluid per unit length is $-\phi_m \nabla_i p = \phi_m \rho_{f_m} \frac{\partial^2 u_i}{\partial t^2}$, or $Q_i^{(m)} = \phi_m \rho_{f_m} \frac{\partial^2 u_i}{\partial t^2}$. From Lagrange's equations, we have $Q_i^{(m)} = \frac{\partial}{\partial t} \left(\frac{\partial T}{\partial \dot{U}_i^{(m)}} \right) = \frac{\partial^2}{\partial t^2} (\rho_{0m} u_i + \rho_{mm} U_i^{(m)}) = (\rho_{0m} + \rho_{mm}) \frac{\partial^2 u_i}{\partial t^2}$. Comparing the above equations, we obtain

$$\phi_m \rho_{f_m} = \rho_{0m} + \rho_{mm}, \quad m = 1, 2. \quad (\text{A13})$$

Since $u_i = U_i^{(m)}$, the kinetic energy becomes $T = \frac{1}{2} \sum_{i=1}^3 (\rho_{00} + 2 \sum_{m=1}^2 \rho_{0m} + \sum_{m=1}^2 \rho_{mm}) \dot{u}_i^2$.

The total mass of fluid-solid aggregate per unit volume is $\rho = \rho_{00} + 2 \sum_{m=1}^2 \rho_{0m} + \sum_{m=1}^2 \rho_{mm}$. The total density can also be expressed as $\rho = \rho_0 + \sum_{m=1}^2 \phi_m \rho_{f_m} = \rho_0 + \sum_{m=1}^2 (\rho_{0m} + \rho_{mm})$, where ρ_0 is the density of solid skeleton. Comparing the above equations, we obtain

$$\rho_0 = \rho_{00} + \sum_{m=1}^2 \rho_{0m}. \quad (\text{A14})$$

In terms of the tortuosity τ , the density coefficient ρ_{mm} can be written as (Berryman & Wang 2000; Carcione 2015):

$$\rho_{mm} = \tau^{(m)} \phi_m \rho_{f_m}, \quad m = 1, 2, \quad (\text{A15})$$

where $\tau^{(m)} = \frac{1}{2}(1 + \frac{1}{\tilde{\phi}_{m0}})$. We have five unknowns $\rho_{00}, \rho_{0m}, \rho_{mm}$ ($m = 1, 2$) and five equations. Thus, the density coefficients can be determined as

$$\rho_{mm} = \frac{\rho_{f_m}}{2} \phi_m \left(1 + \frac{1}{\tilde{\phi}_{m0}}\right). \quad (\text{A16})$$

$$\rho_{0m} = \frac{\rho_{f_m}}{2} \phi_m \left(1 - \frac{1}{\tilde{\phi}_{m0}}\right). \quad (\text{A17})$$

$$\rho_{00} = \rho_0 - \frac{1}{2} \sum_{m=1}^2 \rho_{f_m} \phi_m \left(1 - \frac{1}{\tilde{\phi}_{m0}}\right). \quad (\text{A18})$$

For the fluid-inside-inclusion (FII) case, the density coefficients are $\bar{\rho}_{22}, \bar{\rho}_{02}$ and ϕ_2, ϕ_{20} are replaced by $\tilde{\phi}_2, \tilde{\phi}_{20}$. For the fluid-outside-inclusion (FCI) case, the density coefficients are $\bar{\rho}_{11}, \bar{\rho}_{01}$ and ϕ_1, ϕ_{10} are replaced by $\tilde{\phi}_1, \tilde{\phi}_{10}$. The density of the solid skeleton ρ_0 is $\rho_0 = \sum_{m=1}^2 \tilde{v}_m (1 - \tilde{\phi}_{m0}) \tilde{\rho}_{s_m}$. Here $\tilde{\rho}_{s_m}$ is the solid mass density average in phase m of the mesoscopic volume, and ρ_{f_m} and Ω_m are the fluid densities and fluid phase volume in each phase, respectively. For the FII case, $\tilde{v}_1 = v_1, \tilde{\phi}_{10} = \phi_{10}, \tilde{\rho}_{s_1} = \rho_{s_1}, \tilde{v}_2 = v_2 + v_3, \tilde{\phi}_{20} = \tilde{\phi}_{20}, \tilde{\rho}_{s_2} = \frac{\rho_{s_1} v_2 + \rho_{s_2} v_3}{v_2 + v_3}$, and for the FCI case, $\tilde{v}_1 = v_1 + v_2, \tilde{\phi}_{10} = \tilde{\phi}_{10}, \tilde{\rho}_{s_1} = \frac{\rho_{s_1} v_1 + \rho_{s_2} v_2}{v_1 + v_2}, \tilde{v}_2 = v_3, \tilde{\phi}_{20} = \phi_{20}, \tilde{\rho}_{s_2} = \rho_{s_2}$.